Design of a High-Efficiency Hydrofoil Through the Use of Computational Fluid Dynamics and Multiobjective Optimization

N. Spogis
ESSS, Engineering Simulation and Scientific Software, Rua do Rocio, 423 10 andar conj.1001/1002, Vila Olímpia, CEP: 04552-000, São Paulo, SP, Brazil

J. R. Nunhez
School of Chemical Engineering, State University of Campinas, UNICAMP, P.O. Box 6066, 13083-970, Campinas, SP, Brazil

DOI 10.1002/aic.11804
Published online May 14, 2009 in Wiley InterScience (www.interscience.wiley.com).

A computational fluid dynamics (CFD) model is proposed, based on ANSYS-CFX tools coupled to optimization models inside the commercial optimization software mode-FRONTIER in order to obtain an optimal design of a high-efficiency impeller for solids suspension. The analysis of impeller shape performance was carried out using the shear-stress transport (SST) turbulence model with streamline curvature correction. This turbulence model combined the advantages of the $\kappa-\varepsilon$ and $\kappa-\omega$ models, ensuring a proper relation between turbulent stress and turbulent kinetic energy, allowing an accurate and robust prediction of the impeller blade flow separation. The multiple frames of reference and the frozen rotor frame change models were used for the rotor/stator interaction inside the mixing vessel. The optimization procedure used seven design variables, two nonlinear constraints and two objective functions. The objective functions chosen (among many other possible options) to evaluate the impeller performance were the maximum solid distribution throughout the vessel (homogeneous suspension) reflected by a low variance between local solid concentration and average solid concentration inside the vessel and the higher pumping effectiveness, which was defined as the quotient of the flow and power numbers. The first objective function searches for impeller configurations able to provide good solid suspension, since it aims to achieve homogeneous suspension. The second objective function aims to reduce power consumption for a high-pumping capacity of the impeller. These criteria were considered enough to characterize the optimized impeller. Results indicated that the optimized impeller presented an increase of the pumping impeller capacity and homogeneous solid suspension with low-power consumption, especially when compared with the PBT 45° impeller. © 2009 American Institute of Chemical Engineers *AIChE J*, 55: 1723–1735, 2009

Keywords: mixing, solid suspension, computational fluid dynamics, stirred tank, optimization, hydrofoil

Correspondence concerning this article should be addressed to N. Spogis at nicolas@esss.com.br and J. R. Nunhez at nunhez@feq.unicamp.br

Introduction

Mixing vessels are widely used in the chemical, petrochemical, pharmaceutical, biotechnological and food processing industries to optimize mixing and/or heat transfer. Mixing must be efficient to ensure optimum product quality.[1,2,3] Variables of interest may include mixing times, gas holdup, power draw, local shear, strain rates and solid distribution.

In the chemical industry, for example, the mixing of reacting substances should occur as fast as possible in order to achieve an efficient reaction and this aspect is often a process problem. In this case, an impeller which produces a highly turbulent flow is needed to reduce segregation and minimize the mass and energy transport limitations for chemical reactions.

In biochemistry, on the other hand, there is a need to suspend microorganisms to improve the efficiency of bioreactors.

Another macro-level mixing aspect is related to how the flow pattern generated by the impeller affects both the solid suspension and particles incorporation and distribution within the vessel. Parameters that affect Liquid-solid mixing are the shape of the solids, solid-size distribution area, solid concentration, solid density, liquid density and viscosity.[1,3,4–12,14]

The quality of solid distribution includes the description of fillets in on and off bottom motions and the uniform solid suspension. These effects are very important in some mixing applications such as in the mining industry, rubber crumb, crystallization and precipitations. Abrasion and impeller wear are important factors to be considered in solid-liquid mixing.[3]

There are also some important economic issues involved. The minimization of the amount of power consumption to ensure certain mixing conditions is one of these issues. The cost of the impeller and vessel materials, and the lifetime of the equipment are also important.[2,3,15]

All the aforementioned aspects depend strongly on the geometry of the impeller, vessel parameters as well as the rotational speed of the stirrer and the fluid properties.[1,3]

The variety of mixing applications has led to a tremendous number of different types of impeller and vessels which are in use at present. Due to the great amount of factors that affect the impeller performance, it is very difficult to select a proper impeller design for a specific process. Experimental investigations are usually very costly and time-consuming. The application of computational fluid dynamics (CFD) results in a faster and lower design cost, reducing experiments and providing a more reliable scale-up.[22] This also gives a better understanding of processes, leading to higher yields and reduced waste.In this study, the numerical investigation of the flow of a stirred vessel using a CFD approach coupled with a multiobjective design optimization method is presented, and results indicate that it can be a very useful tool offering new possibilities for higher product quality, cost reduction and power consumption minimization.

The ANSYS CFX software was chosen for the numerical CFD results. ANSYS ICEM CFD was chosen for the geometry and mesh generation process in order to provide sophisticated geometry acquisition, mesh generation, mesh editing and a wide variety of solver outputs. The built-in geometry creation of the mesh generating software (automatically done following the mesh constraints specification), its highly automated batch processing and the scripting framework for the batch preprocessing, processing and post-processing operations were incorporated inside modeFRONTIER.[23] In other words, after defining all the impeller specifications, all these tools work together generating the geometry of an impeller obtained by the optimization procedure followed by the mesh generation, model simulation and post processing of the most important results. All these steps were done for every geometry until the optimum geometry was found following the model constraints. The complete procedure is carried out by the model without any further human intervention.

The optimization software ModeFRONTIER is composed of models that range from gradient-based methods to genetic algorithms.[24–26] It allows the specification of the two objective functions used to design the impeller namely: (1) the minimization of the concentration variance inside the vessel, and (2) the maximization of the impeller efficiency, defined by the quotient (flow number/power number). Factors that influence the impeller geometry were successfully investigated using this tool. This optimization software in effect became a link between the CAE tools (ICEM and CFX) optimizing the procedure by modifying the value assigned to the input variables (design parameters and flow requirement), and monitoring the outputs. The section entitled ''Preliminary investigations'' explains the optimization procedure in more detail.

Basic Numerical Concepts

In the following sections, a brief introduction to the CFD model is presented and a description of the employed numerical tools is also given. Then the coupling of the models within the commercial program (modeFRONTIER) is also considered.

Governing equations for fluid flow

The set of equations solved numerically by ANSYS CFX were the unsteady Navier-Stokes equations in their conservation form and the mass conservation equation. It also used the alternate rotation model that solves numerically the absolute frame velocity instead of the relative velocity.

The frozen rotor model was used in a 120° sector of the reactor. The shear-stress transport (SST) turbulence model was used since it is more accurate and robust for the prediction of problems involving flow separation. This aspect is important in this project since it is paramount that no boundary layer separation exists in the optimized impeller.[27–29]

Vessel Parameterization A schematic representation of the vessel configuration is shown in Figure 1. The system consists of a torispherical-bottomed cylindrical vessel with diameter T and height H, which equals the height of the liquid. The off-bottom clearance is constant and equals H/4.

The torispherical 100-6 head has a crown radius of 100% (or equal to) the diameter of the head with a knuckle radius of 6% of the diameter of the head. The shaft of the impeller is concentric with the axis of the vessel. The actual geometrical parameters, which are considered as a standard configuration, are summarized in Figure 1. The fluid is water at 25°

Parameters	Parameter Value
Tank diameter	T = 1m
Height of the liquid	H= T = 1m
Bottom clearance	C=H/4 = 0.25m

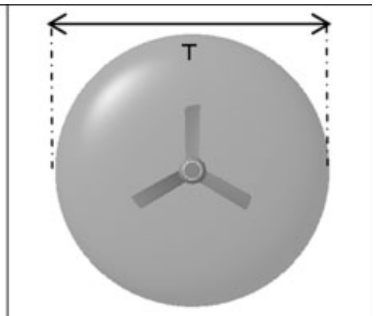

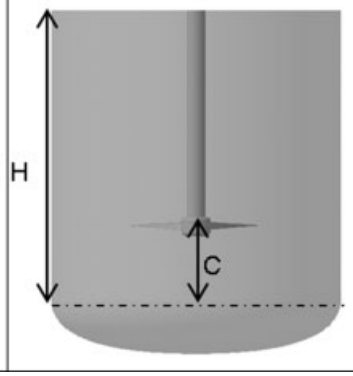

Figure 1. Schematic representation of the stirred tank studied in this work.

C, with density $\rho = 997.0$ kg/m^3, and viscosity $\mu = 0.8899$ cP.

Impeller Design Variables and Meshing The optimization of the impeller blades requires a representation of the blade that should be flexible enough to produce a very wide range of impeller shapes. Conversely, it should use the minimum number of variables possible to save computational time and to allow an efficient storage and manipulation of the data for a wide variety of viable breeding population of candidate impellers.

Changes on the efficiency of the impeller are produced by a wide number of factors, namely: adjustments to the helix angle, the angle between the resultant relative velocity and the blade rotation direction, and also to the blade pitch. Very small pitch and helix angles give a good performance against resistance, but provide little thrust and also little pumping. Larger angles have the opposite effect.

The best helix angle is when the impeller blade is acting as a wing producing much more lift than drag, roughly 45° in practice. However, due to the shape of the impeller, only part of the blade can actually be operating at peak efficiency. The outer part of the impeller blade produces the most pumping, and so the blades are positioned at a pitch that gives optimum angle to that portion. Since a large portion of the blade is, therefore, at an inefficient angle, the inboard ends of the impeller blade are hidden by a streamlined spinner to reduce the resistance torque that would otherwise be created. Very high-efficiency pumping impellers are similar. They need an optimum angle of attack in its airfoil section to work properly. An impeller working at a pitch angle of 45° at high-rotational speeds, presents a very high-angle of attack. There is a need to adjust the impeller pitch angle to alter resistance to torque and improve efficiency. A further consideration is the number and the shape of the blades used. Increasing the aspect ratio of the blades reduces drag. However, the amount of pumping produced depends on the blade area, so using high-aspect blades can lead to the need of an impeller diameter which is unviable.

A further balance is that a small number of blades reduces the interference between blades, but there is a need of a sufficient total blade area to suspend the solids, so a compromise between these opposing effects is needed. Increasing the number of blades also decreases the amount of work each blade is required to perform.

A schematic representation of the impeller configuration is shown in Figure 2. For the model of this work, the impeller blade can be represented by seven construction parameters, which are even able to allow a twisting of the blade. The parameters are:

1 Impeller diameter ratio;
2 Root chord;
3 Tip chord;
4 Root chord angle;
5 Tip chord angle;
6 Root profile;
7 Tip profile.

Two of these parameters are discrete variables (root and tip profile) and five are continuum variables. Table 1 shows the range of variation of these parameters. All the variables defined above were changed in a range of values to allow a great number of candidate numerical prototypes to be tested in the optimization procedure (the ranges were determined based on the values used for commercial impellers).

This new hydrofoil impeller was designed to maximize solid dispersion in stirred vessels at the lowest possible power consumption.

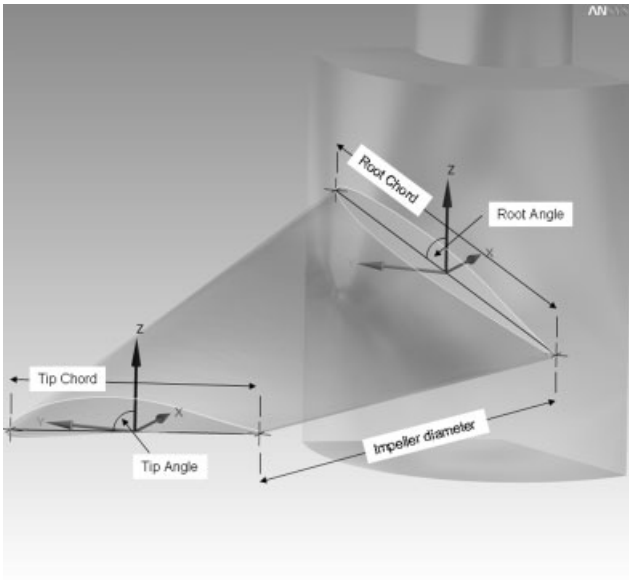

Figure 2. Schematic representation of the impeller with the variables used in the optimization procedure.

A note should be made that the power number of the impeller determined in this work could lead to a working condition that might not be ideal for some industrial use. The commercial hydrofoils have a power number which are normally higher than 0.1 to guarantee a wide range of use. Therefore, commercial hydrofoils have a power number higher than the power number of the impeller obtained in this work through the optimization procedure. The model developed in this work does not use this value of power number as a lower limit. Further work may take this aspect into consideration for selection of geometries for general industrial use.

Since avoiding flow separation is an important aspect of this work, several airfoil shapes were studied. An airfoil with the shape of a wing is seen at its cross-section in Figure 3. It is passed through a fluid in order to provide either lift or down force, depending on its application. This force is generated by a pressure gradient. The pressure gradient and the impeller blade size are responsible for the impeller pumping.

Subsonic and low-Reynolds airfoils have a characteristic shape. It starts with a rounded leading edge, followed by a sharp trailing edge, often with camber. A comprehensive source of low-speed airfoil geometries and performance data is provided by Goparathnam and Selig[30] at the University of Illinois at Urbana-Champaign (UIUC). Other works are Xu and Sankar,[31] Lyon et al.[32] and Caradonna and Tung.[33]

The criteria adopted for the airfoil selection in this study are: high lift at a low angle of attack, high C_{lmax}, gentle stall characteristics, relative low coefficient of moment, sufficiently low drag, easy manufacturability and good operations at low Reynolds number.

Based on these criteria, four possible airfoils were selected and used as root and tip blade airfoil parameters, as shown in Figure 3.

One of the most important aspects of the model of this work is that it needs to predict with accuracy the boundary layer on the impeller blade, which makes paramount the choice of the turbulence model. The SST turbulence model with curvature correction was chosen to properly predict the boundary layer behavior. Two criteria need to be respected in order to generate meshes which satisfy the minimal requirements for accurate boundary layer predictions:

- Minimum spacing between walls and first node in the boundary layer.
- Minimum number of nodes in the boundary layer.

The mesh near the wall followed size restrictions. The size of the layer of control volumes at the wall are predicted by simplifications of laminar boundary layer equations for flat plates. Respecting these requirements, fundamental for a correct prediction, a tetrahedral mesh was generated. A smoothing algorithm was chosen in order to provide high element quality (avoiding distorted control volumes). The accuracy of calculation was improved by placing a thin layer of prism elements near the walls. The mesh generated is shown in Figure 4.

Numerical principles of the optimization method

It is well known that classical gradient-based algorithm methods use the ''direction of improvement'' information in order to achieve a fast and accurate convergence toward the optimal solution. It requires an accurate gradient evaluation.

Holland[34] is generally credited for the creation of the genetic algorithm model, and he gives an introduction to this method in Holland.[34] He points out that the success of this computational method, which uses optimization techniques such as simple hill climbing, is due to its ability to properly use *partial solutions* in the optimization problem. ModeFRONTIER has implemented an improved version of multiobjective genetic algorithm (MOGA-II). It uses a smart multisearch algorithm for robustness and directional crossover for fast convergence. The efficiency of the method is ruled by its reproduction operators: classical crossover, directional crossover, mutation and selection.[35]

This project employed the multiobjective genetic algorithm to determine a Pareto optimal set of impeller blade designs, with each member offering a unique trade-off between conflicting objectives of low-energy consumption, increasing the impeller pumping capacity and improving tank homogeneity. The Pareto optimal design consists of all

Table 1. Input Variables

Variable	Minimum Value	Maximum Value	Discrete/Continuum
Impeller diameter	0.4	0.5	Continuum
Root chord	0.2	0.2	Continuum
Tip chord	0.1	0.2	Continuum
Root chord angle	20 degrees (related to rotation axis)	70 degrees (related to rotation axis)	Continuum
Tip chord angle	30 degrees (related to rotation axis)	95 degrees (related to rotation axis)	Continuum
Root profile	DAE11, S1223, E387, FX 63-137		Discrete
Tip profile	DAE11, S1223, E387, FX 63-137		Discrete

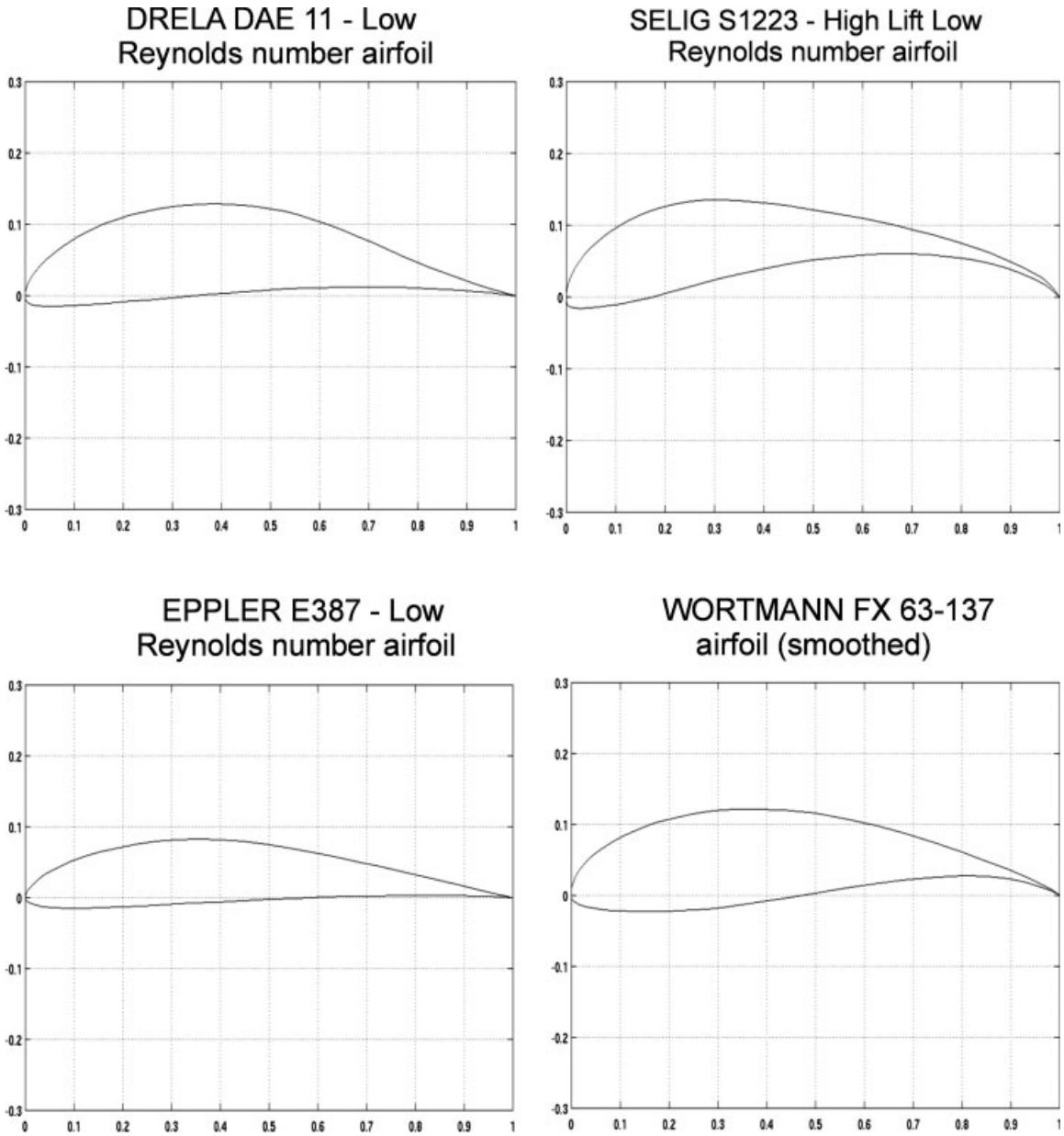

Figure 3. Four different airfoils used for low Reynolds number applications.

the nondominated solutions possible in the N-dimensional parameter domain being considered, and forms an N-dimensional surface.

Control program

The components described in the preceding sections are integrated and coupled to modeFRONTIER optimization software, which is illustrated schematically in Figure 5.

The optimization procedure involves the following major steps:

1 **Optimizer:** The optimizer is started and computes a new set of design variables. Afterward it is turned on stand by.

2 **Geometry and Grid generation.** On getting the signal that the new design variables are available, the grid generation tool (ANSYS ICEM CFD) becomes active and creates the new geometry and the corresponding numerical grid.

3 **Flow simulation:** Np estimation: The solver computes the flow field and estimates the power number Np when it gets the signal that the new grid is available. This simulation is made using a steady state approach.

4 **New rotation computation**: The value of the power number Np estimated for the geometry normally provides power consumption different from the 2 kW/m^3 criteria chosen in this work. With the knowledge of the impeller diameter and the fluid density, a new rotational velocity is calculated in order to conserve the power consumption. This procedure is described in the next section entitled Power Consumption Conservation.

5 **Steady-state flow simulation:** With the new rotation velocity, a new steady-state simulation is performed in order

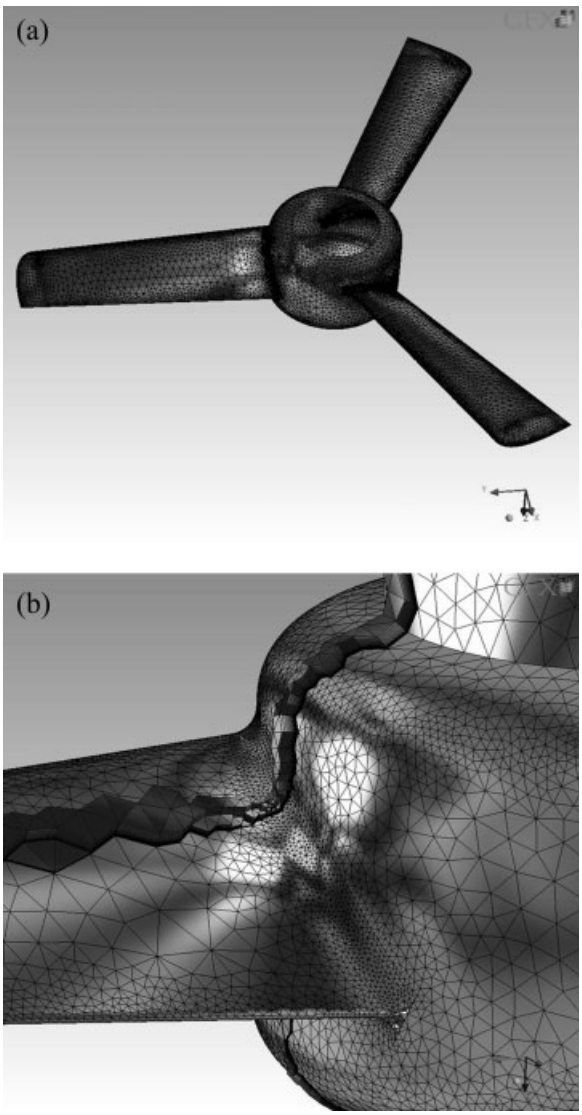

Figure 4. An example of a mesh generated in this work using adaptive meshing.

to determine a starting value for the next step that will determine the solid distribution. The flow number Nq is also estimated with the new rotational speed.

6 **Transient solid dispersion:** Estimates the solid distribution within the stirred vessel.

7 **Post process results:** In this step ANSYS CFX-Post computes the output variables and objective functions for the new geometry, and writes them in an output ASCII file of modeFRONTIER.

8 **Test of optimizer convergence:** The optimizer decides, by the given criteria, if the current value of the objective functions should be accepted as optimum. If it is confirmed, the procedure is finished, if not, the procedure is automatically repeated from step 1.

Power Consumption Conservation

Scale-up based on equal power per volume P/V, is probably the most accepted criteria in mixing because it is easily understood and practical. It is certainly more conservative than the impeller tip speed criteria, which is also widely used.

As the vessel volume in this optimization procedure is constant, it is only necessary to maintain the power consumption constant. As the impeller geometry is not constant, the power number (Np) is not constant either, so rotational speed corrections are needed in order to maintain the power consumption constant.

A power consumption of 2 kW/m^3 is used in this work to heavy solid suspension processes. This value is a rule of thumb. However, it is true in many industrial applications. This fixed value was chosen for the optimization process, so the different impellers generated could be compared only in terms of characteristic flow and its capacity to homogenize the stirred vessel.

The following algorithm was used for steps 3 to 5 of the optimization procedure to maintain the same power consumption.

1 Evaluate the torque

2 With the blade torque and initial rotational velocity, calculate the Power consumption: $P = \overline{\omega}.\mathrm{T}$

3 With the power consumption, fluid density, initial rotation velocity and impeller diameter, calculate the power number: $Np = \frac{P}{\rho.N^3.D^5}$

4 With the power number, impeller diameter, fluid density and the desired power consumption, a new rotational speed is calculated and used in the step 5 of the optimization procedure: $N = \sqrt[3]{\frac{P}{\rho.D^5.Np}}$

Constraints

Constraint handling is an integral part of any general parameter of an optimization method. In order to restrict the solution to a limited area, only two of the defined constraints

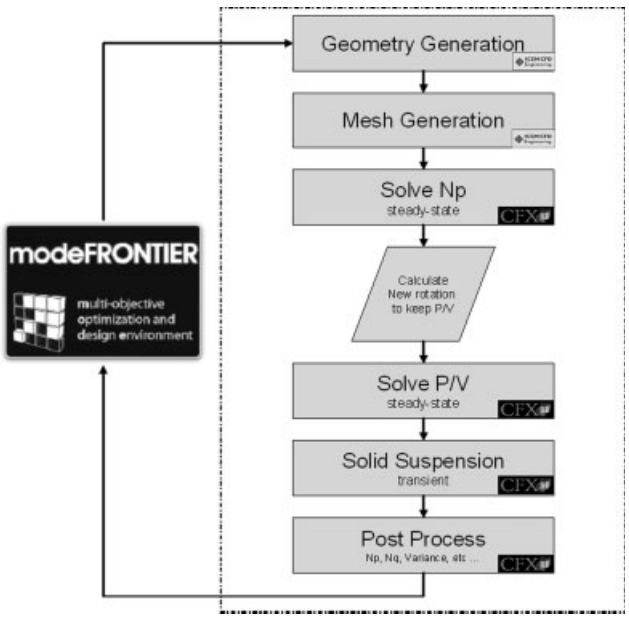

Figure 5. Schematic Diagram of the optimization procedure.

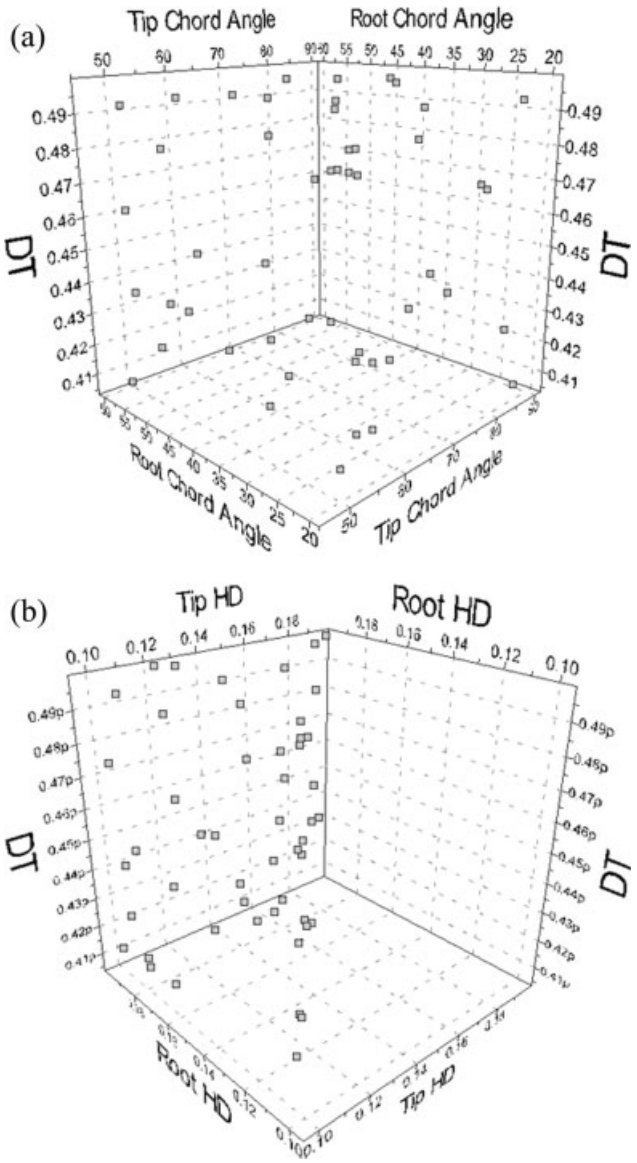

Figure 6. Population distribution in the design space for the initial impellers used for the optimization method.

relate specifically to the creation of ''realistic impeller blades'' in the optimization problem:

- Tip chord angle **<=** root chord angle.
- Tip chord <= root chord.

The angles of the root and tip chord vary, so the CAD generating model create the surface using a linear interpolation of the values of the angles starting at the hub (root chord), and finishing at the impeller tip (tip chord). The width of the blade is also an interpolation of the values of the root chord and tip chord. The final surface is obtained by the CAD model using a loft surface.

Output variables and objective functions

Ten output variables were used to monitor the mixing efficiency but only two of them were used as objective functions, which are the pumping effectiveness (quotient of the flow and power numbers) and the vessel solid concentration variance. The pumping effectiveness was maximized and the vessel solid concentration variance was minimized.

The solid concentration variance of the vessel was estimated by the well known statistical formula

$$s^2 = \frac{1}{n-1}\sum_{i=1}^{n}(C_i - \overline{C})^2 \tag{1}$$

Where n is the number of nodes in the mixing vessel mesh. As Eq. 1 shows, a truly complete homogeneous solid suspension would provide $s^2 = 0$. Therefore, the optimized impeller has a low variance.

The pumping effectiveness is defined as

$$\xi = \frac{N_q}{N_P} \tag{2}$$

The higher the pumping effectiveness is, the higher the pumping capacity will be for small power consumption.

Numerical Results

In the next sections, a description is given of the grid requirements followed by a discussion of the preliminary investigations of the design space. These sections propose a strategy to reduce computational errors and minimize the computational time required to optimize and design the high-efficiency hydrofoil prototype.

Grid requirements

In order to predict turbulence properly, it is important to have at least a layer of control volumes capturing the effect of the boundary layer, which is assessed by the dimensionless variable y^+. Studies of the sensitiveness of y^+ value in the impeller for values between 0.001 and 1 show that there is almost no effect of these changes on the final solution. Once the maximum y^+ increases to values above 10, the transition location of the boundary layer begins to move upstream. At a maximum y^+ of 25, the boundary layer is almost completely turbulent. Preliminary investigations also indicate that for y^+ values below 0.001, the transition location appears to move downstream. This is presumably caused by the large surface values of the specific turbulence frequency, which increases proportionally with the height of the first grid point.

The effect of expansion ratios of the wall for a y^+ value of 1 was studied in order to determine the number of cells in the boundary layer. Expansion factors between 1.05 and 1.1, present no effect on the solution. For larger expansion factors between 1.2 and 1.4, there is a small, yet noticeable upstream shift in the transition location.

The effect of the streamwise grid refinement shows that the model was not very sensitive to the number of streamwise nodes. The grid independent solution appears to occur when there are approximately 80 streamwise grid points.

Preliminary investigations

A preliminary investigation was carried out to determine the behavior and the main characteristics of the problem that

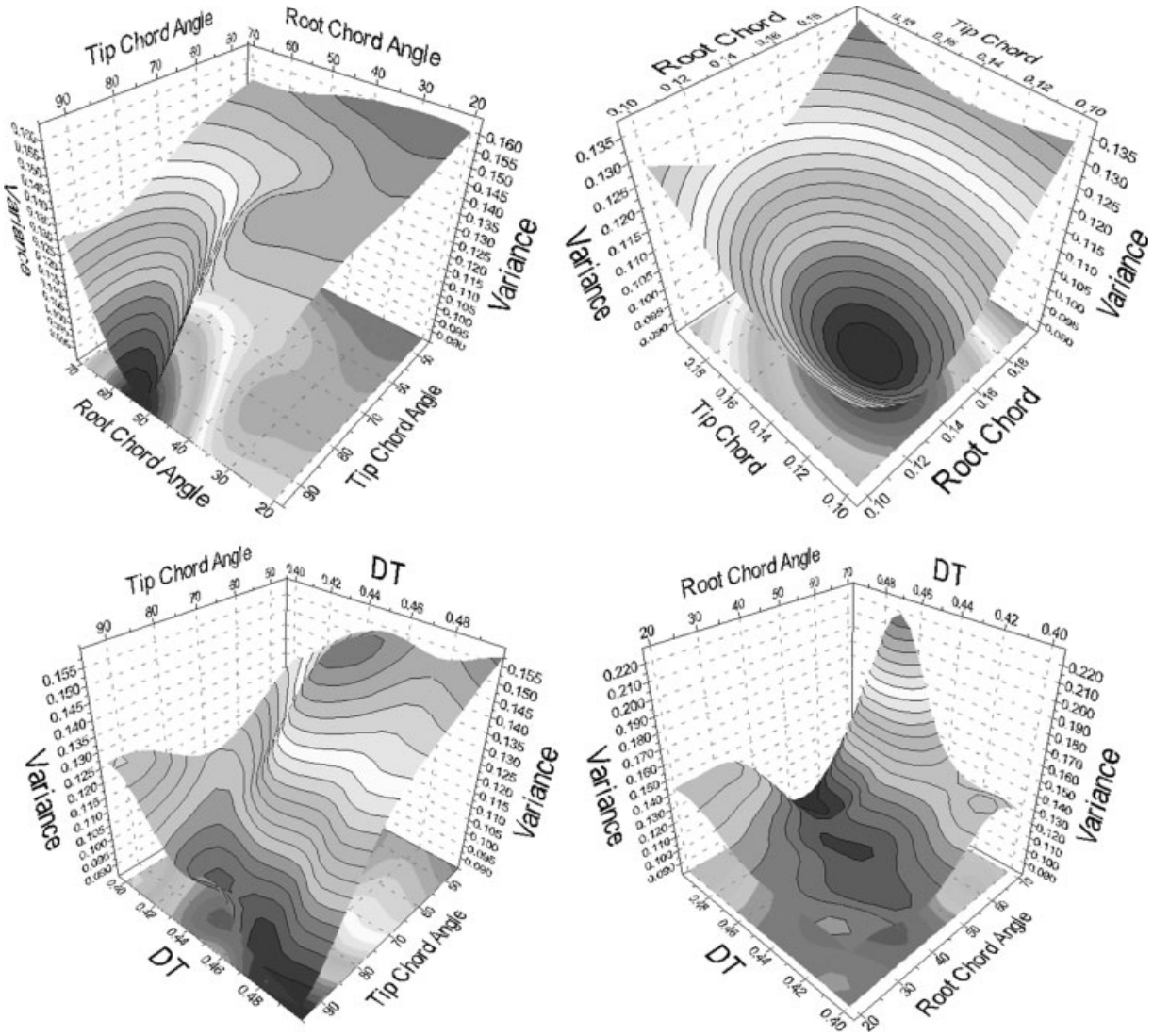

Figure 7. Response surfaces of the optimization procedure for the variance of the solid concentration inside the vessel.

is being examined. The aim is to analyze which variables affect most the problem. The distribution of the initial impellers and their variation on the design space is shown in Figure 6.[36,37]

Initial 2-D (two-dimensional) CFD studies show that the DAE 11 airfoil provide a better lift/drag relationship, and have a gentle stall behavior when compared to the other airfoils studied. Therefore, in order to minimize the number of input parameters and reduce the computational time requirements, the root profile and the tip profile was fixed as the DAE 11.

Figure 7 shows the relationship between the solid concentration variance and the input parameters (root chord angle, tip chord angle, impeller diameter, root chord and tip chord). Figure 7a indicates that for a minimum variance (one of the objectives of this work) the interaction between the tip chord angle and the root chord angle indicates that the tip chord angle should be around 90° or a little over, and the root chord angle should be around 50 and 55°. Figure 7b shows the interaction between the root chord size and the tip chord size as a function of the variance. The surface presents a minimum and it indicates a root chord and tip chord around 15 cm. The interaction between the D/T ratio and tip chord angle in Figure 7c also shows a minimum for a small variance. The tip chord angle is again around 90° and the D/T ratio is around 0.5. Figure 7d shows the D/T ratio interaction with the root chord angle. In this case there is more than one minimum for a small variance. The root chord angle should be between 40 and 55 and the D/T ratio between 0.46 and 0.5.

Figure 8 shows the relationship between the impeller pumping effectiveness and the input parameters (root chord angle, tip chord angle, impeller diameter, root chord and tip chord). In this case the aim is to achieve a high pumping effectiveness. Figure 8a presents the maximum impeller effectiveness for a tip chord angle around 90°, and a root chord angle around 70°. Figure 8b shows that the maximum pumping effectiveness is for a 19 cm root chord size and a

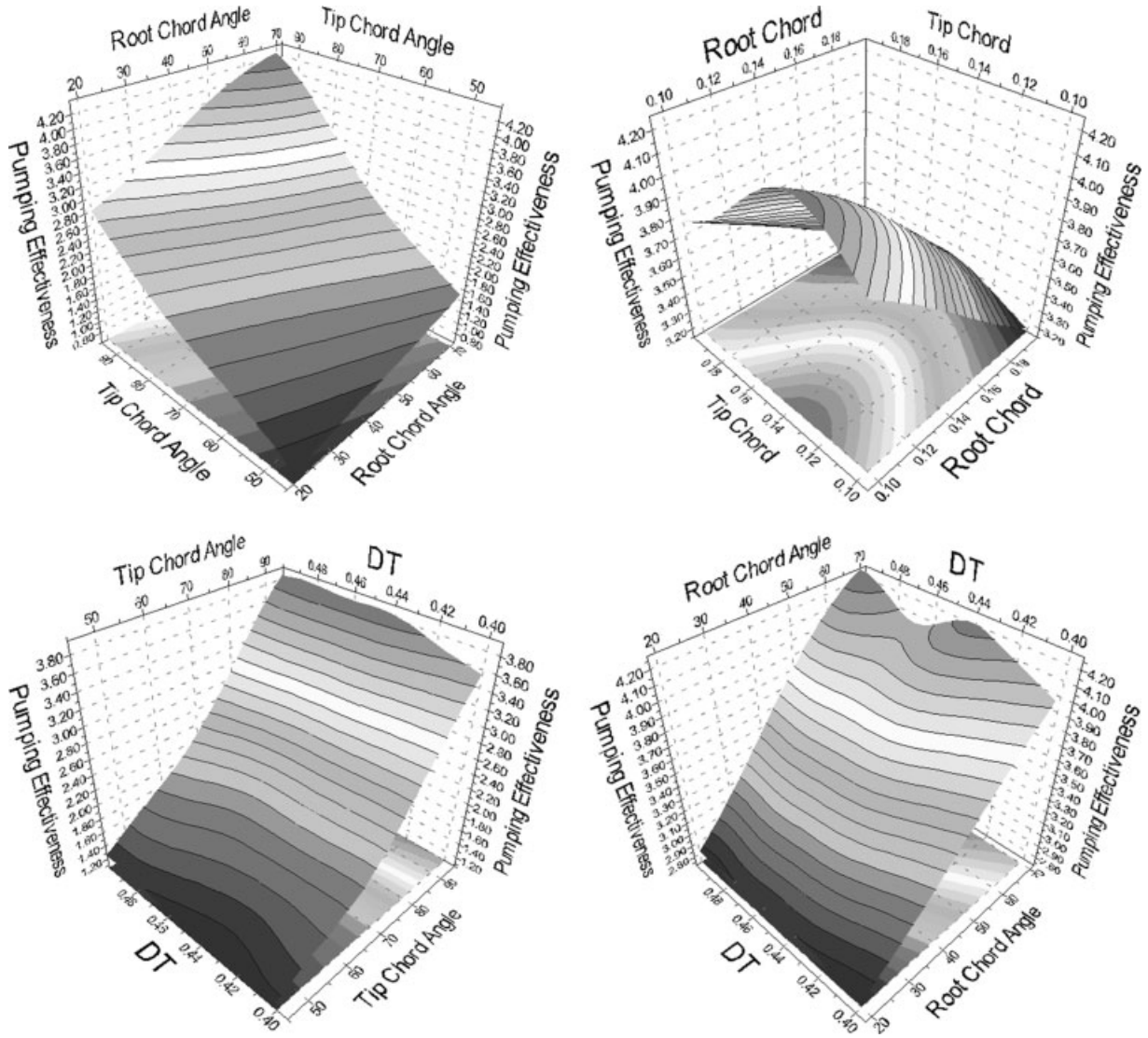

Figure 8. Optimization response surfaces for pumping effectiveness.

tip chord size around 13.5 cm. The interaction between the D/T ratio and tip chord angle in Figure 8c also shows that the maximum for the tip Chord angle is again around 90°, and the D/T ratio is around 0.44 and 0.5. Figure 8d shows the D/T ratio interaction with the root chord angle. In this case there is more than one maximum at the response surface. The root chord angle should be around 70°, and the D/T ratio range between 0.44 or 0.5.

Optimization Results

It is important to mention that the computational requirements for one optimization step (one impeller design) took approximately 5.2 h of computing time on a two processor AMD Athlon™ MP 2800+ machine, 2 GB RAM. The optimization process was configured so as to guarantee the robustness of the calculation. The optimization method arrived at some very interesting results, and it required only 15 generations of 30 individuals (450 optimization cycles), which resulted in about 98 days of computing time.

The performed evaluations allowed for the establishment of a general tendency and for the definition of the influence of each parameter on the estimated values. Furthermore, an experimental validation was performed (the results will be discussed in the following section), and the solid concentration variance was reduced by 48.5%, the power consumption reduced by 84.4%, and the pumping effectiveness increased by 410.2%, when compared to the performance of a pitched blade impeller (also with a DAE 11 blade profile).

The initial pitched blade impeller (constant tip chord angle − 45°), has a low-discharge angle and low-solid suspension. The pumping effectiveness is low due to the radial velocity component of the PTB45. The generated flow shows a boundary layer separation and there is a blade stall due to the high tip chord angle.

Figure 9a shows the velocity contour plot and the velocity vector plot for the PBT45. It can be easily noticed that the

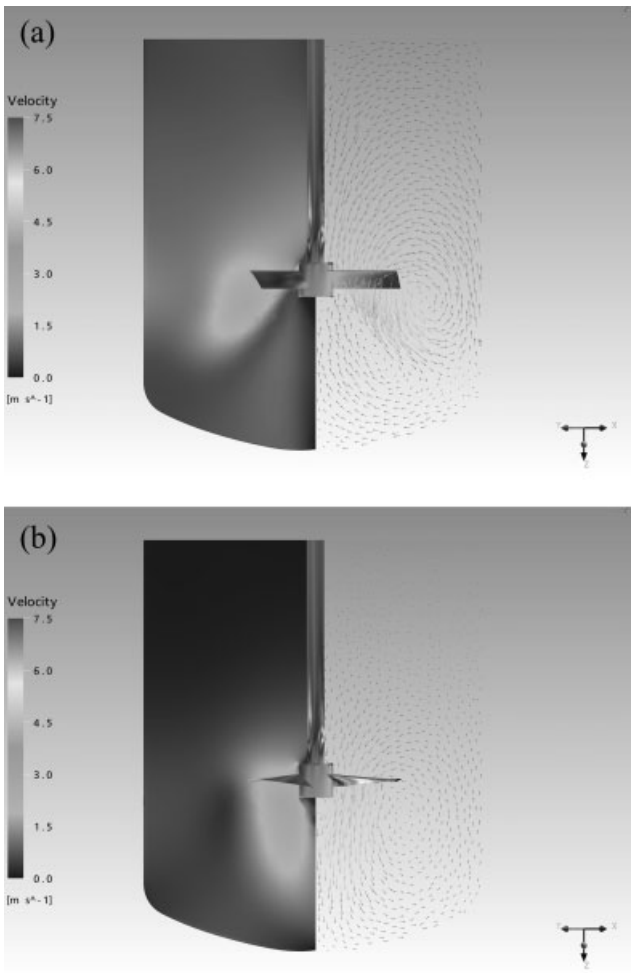

Figure 9. Velocity for the 45° pitched blade and optimized Impellers.

PBT does not have a pure axial flow. This fact has already been mentioned before in the literature and can even change the pattern of the PBT 45° (see, for example, Kresta and Wood[38]). Due to that, there is a poor solid suspension in the region below the impeller, as can be noticed in Figure 10a.

Figures 9b shows that the optimized impeller has a very strong axial flow, resulting in a higher pumping effectiveness and, consequently, a higher solid suspension, as shown in Figure 10b. It can be noticed that the solid concentration at the bottom of the vessel is very low, resulting in a low variance, which is the characteristic of a very well homogenized suspension.

It can be said that the optimization procedure resulted in an impeller with a very pure axial flow below the impeller. It makes sense since a pure axial flow results in a flow direction which minimizes solid settling at the bottom of the vessel (low variance as specified by the optimization constraint). The optimized impeller has only a very small region with boundary layer separation, just a small point near the hub and it shows a very low-tip vortex, when compared to the PBT 45°. It also makes sense, since this shows that no energy consumption is lost in vortex generation or radial flow. The energy is only for axial pumping, which is the objective of the work specified in the optimization procedure by a higher pumping effectiveness.

After the optimization steps using modeFRONTIER, a further refinement on the impeller tip was done. It was tapered as most high-efficiency impellers are. The objective functions input into the optimization model do not account for this kind of refinement. A smooth joining between the impeller blade and the hub was also designed to reduce the boundary layer separation on this region and improve the blade suction. These changes improved the impeller performance as expected. The final impeller design is shown in Figure 11. It is important to notice that the results in Figure 10 do not show the tapering of the impeller tip.

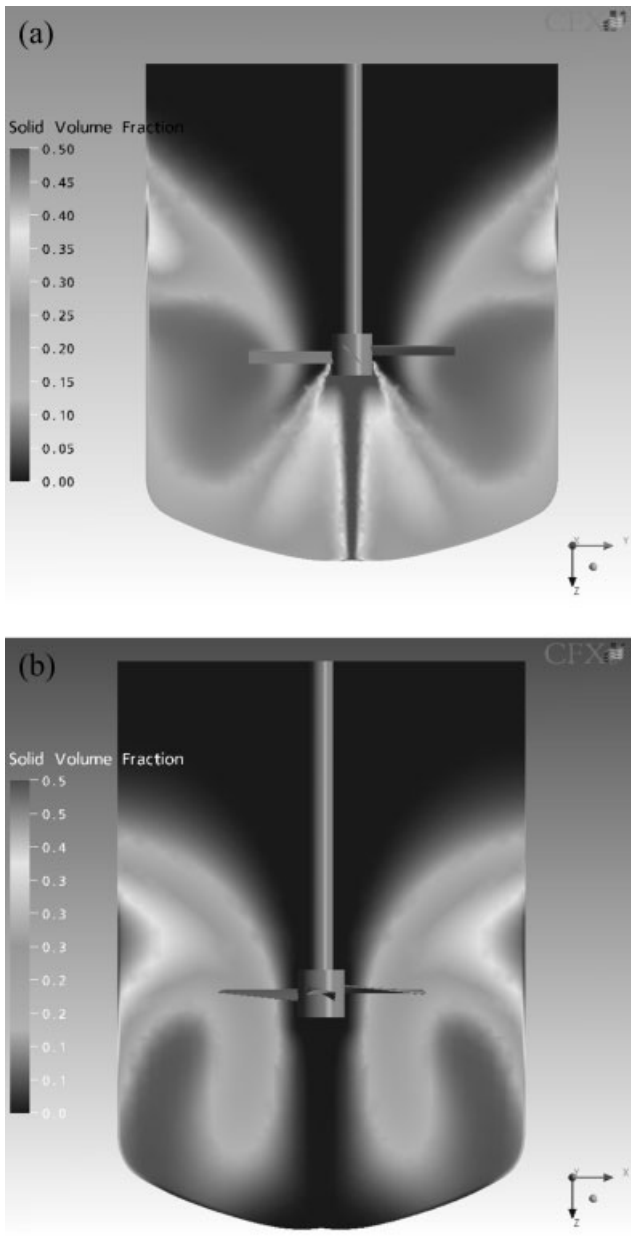

Figure 10. Solids distribution for the 45° pitched blade and optimized impellers.

Figure 11. Optimized blade design.

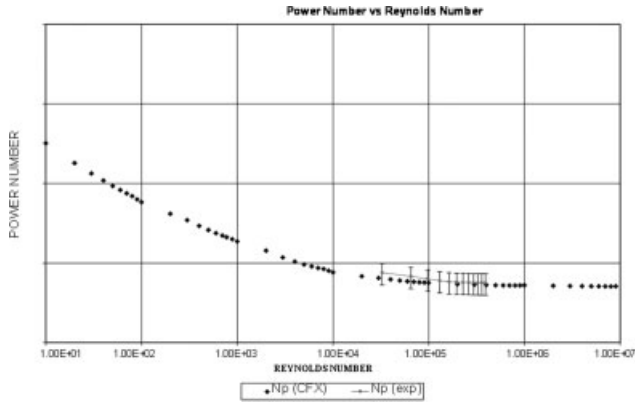

Figure 13. Comparison between computational and experimental results.

Experimental Tests

In order to validate the CFD/Optimization model, some experimental tests were performed. Figure 12 compares two situations in which the optimized impeller performed much better than the PBT impeller. The first two figures in Figure 12 show that for the same power input of approximately 6 W, the optimized impeller suspended much more solids than the PBT impeller. For a power input of 11 W, it can be noticed that both impellers are suspending the solids, but the optimized impeller is suspending much more solids. Figure 13 shows the power consumption obtained by the CFD model and the experimental tank. The results are very similar in the region where experimental results were obtained.

Summary and Conclusions

This multiobjective optimization model for an optimal impeller design contains many innovative elements. It is

Figure 12. Experimental comparison between proposed impeller and the PBT impeller.

believed that the incorporation of parameterization refinements such as tip construction and smoothness of the impeller surface helped in achieving better results.

This research shows that an optimization process is viable to determine promising impeller designs and a brief outline of the methodology to achieve that purpose has been presented.

This work also indicates the advantages of coupling computational fluid dynamics and multiobjective design optimization methods.

Acknowledgments

The authors would like to thank all colleagues of ESSS and Esteco, who helped in the development of this work and also provided the software licenses used in this project, and CenPRA, that kindly manufactured the impeller prototypes.

Notation

Throughout this article, dimensions are given in terms of the fundamental magnitudes of length (L), mass (M), time (T). This section lists symbols used in this article, their meaning, dimensions and, where applicable, their values. Dimensionless quantities are denoted by 1. The values of physical constants (or their default values) are also given.

Symbols

$C\varepsilon 1$ = k-ε turbulence model constant, dimensions 1, value 1.44
$C\varepsilon 2$ = k-ε turbulence model constant, dimensions 1, value 1.92
$C\mu$ = k-ε turbulence model constant, dimensions 1, value 0.09
E = constant used for near-wall modeling, dimensions 1, value 9.793
$\boldsymbol{g}$ = gravity vector, dimensions L T^{-2}, value 9.81
k = turbulence kinetic energy per unit mass, dimensions L^2 T^{-2}
Pk = shear production of turbulence, dimensions M L^{-1} T^{-3}
p, $p$stat = static (thermodynamic) pressure, dimensions M L^{-1} T^{-2}
$p$ref = reference pressure, dimensions M L^{-1} T^{-2}
$p$tot = total pressure, dimensions M L^{-1} T^{-2}
p' = modified pressure, dimensions M L^{-1} T^{-2}
Re = Reynolds number, dimensions 1
$\boldsymbol{r}$ = location vector, dimensions L
$\boldsymbol{SM}$ = momentum source, dimensions M $L^{-2}T^{-2}$
Sct = turbulent Schmidt number, dimensions μt/Γt, value 1
$\boldsymbol{U}$ = vector of velocity **U**x,y,z, dimensions L T^{-1}
U = velocity magnitude, dimensions L T^{-1}
$\boldsymbol{u}$ = vector of fluctuating velocity component **u**x,y,z = turbulent flow, dimensions L T^{-1}
ε = turbulence dissipation rate, dimensions L^2 T^{-3}
ξ = impeller pumping effectiveness
ζ = bulk viscosity, dimensions M L^{-1} T^{-1}
κ = Von Karman constant, dimensions 1, value 0.41
μ = molecular (dynamic) viscosity, dimensions M L^{-1} T^{-1}
μt = turbulent viscosity, dimensions M L^{-1} T^{-1}
μeff = effective viscosity, $\mu+\mu$t, dimensions M L^{-1} T^{-1}
ρ = density, dimensions M L^{-3}
σk = turbulence model constant for the k equation, dimensions 1, value 1.0
$\sigma\varepsilon$ = k-ε turbulence model constant, dimensions 1, 1.3
σw = k-ω Turbulence model constant, dimensions 1, 2
τ = shear stress or sub-grid scale stress, dimensions M L^{-1} T^{-2}
ω = angular velocity, dimensions T^{-1}
y^+ = Y plus 1
P = power consumption
N = rotational speed, dimensions T^{-1}
Np = power number, dimensions 1
Nq = pumping number, dimensions 1
D = impeller diameter, dimensions L
T = tank diameter, dimensions L
C = bottom clearance, dimensions L
H = height of the liquid, dimensions L

Literature Cited

1. Joaquim Jr CF, Cekinski E, Nunhez JR, Urenha LC. *Agitação e Mistura na Indústria*. 1st ed. Rio de Janeiro, Brazil: LTC Editora; 2007.
2. Oldshue JY. *Fluid Mixing Technology*. 1 ed. New York: McGraw Hill; 1983.
3. Paul EL, Atiemo O, Kresta SM. *Handbook of Industrial Mixing, Science & Practice*. 1st ed. Hoboken, NJ: John Wiley & Sons, Inc; 2004.
4. Fasano JB, Bakker A, Penney WR. *Advanced impeller geometry boosts liquid agitation. Advanced liquid agitation. Chemineer Chem Eng*. May 1999.
5. Myers KJ, Bakker A. Solids suspension with up-pumping pitched-blade and high-efficiency impellers. *Can J Chem Eng*. 1998;76:4233–440.
6. Pantula PRK, Ahmed N. Solids Suspension and Gas Holdup in Three Phase Mechanically Agitated Reactors. In: *Chemeca '98*, Port Douglas, Queensland, Australia, 1998. Paper No. 132.
7. Pantula PRK, Ahmed N. The Impeller Speed Required for Complete Solids Suspension in Aerated Vessels: A Simple Correlation? In: *Récents progres en genie des procédés (Mixing IX)*, Paris, France; 1997:11–18.
8. Ibrahim S, Nienow AW. Particle suspension in turbulent regime: the effect of impeller type and impeller/vessel configuration. *Trans IChemE*. 1996;74(A):679–688.
9. Hicks MT, Myers KJ, Bakker A. Cloud height in solids suspension agitation. *Chem Eng Commun*. 1997;160:137–155.
10. Drewer GR, Ahmed N, Jameson GJ. Suspension of High Concentration Solids in Mechanically Stirred Vessels. IChemE Symp. Series. No. 136. Proceedings of the 8th European Conference on Mixing. 1994:41–48.
11. Nienow AW. *The Suspension of Solid Particles*. In: Harnby N, Edwards MF, Nienow AW, eds. *Mixing in the Process Industries*. 2nd ed. London, U.K: Butterworths; 1992:364–393.
12. Nienow AW, Konno M, Bujalski W. Studies on Three-phase Mixing: A Review and Recent Results. In: *Proceedings of the 5th European Conference on Mixing*. Wurzburg, West Germany; 1985:1–13.
13. Weetman RJ, Coyle CK. The Use of Fluidfoil Impellers in Viscous Mixing Applications. AIChE 1989 Annual Meeting, San Francisco, CA; Nov. 5–10, 1989.
14. Buurman C, Resoort G, Plaschkes A. Scaling-up rules for solids suspension in stirred vessels. *Chem Eng Sci*. 1986;41:2865–2871.
15. Rushton JH, Costich EW, Everett HJ. Power characteristics of mixing impellers Part II. *Chem Eng Prog*. 1950;46(9):467–476.
16. Wu JY, Zhu PC, Pullum L. The effect of impeller pumping and fluid rheology on solids suspension in a stirred vessel. *Can J Chem Eng*. 2001;79:177–186.
17. Wu JY, Zhu PC, Bandopadhayay L, Pullum PC, Shepherd IC. Solids suspension with axial flow impellers. *AIChE J*. 2000;46:647–650.
18. Rewatkar VB, Raghava Rao KSMS, Joshi JB. Critical speed for solid suspension in mechanically agitated three-phase reactors: 1. Experimental part. *Ind Eng Chem Res*. 1991;30:1770–1784.
19. Raghava Rao KSMS, Rewatkar VB, Joshi JB. Critical impeller speed for solid suspension in mechanically agitated contactors. *AIChE J*. 1988;34:1332–1340.
20. Wong CW, Wang JP, Huang ST. Investigations of fluid dynamics in mechanically stirred aerated slurry reactors. *Can J Chem Eng*. 1987;65:412–419.
21. Zwietering TN. Suspending of solid particles in liquid by agitators *Chem Eng Sci*. 1950;8:244–253.
22. Aidari AH, Bakker A, Oshinowo LM. Realize greater benefits from CFD. *Chem Eng Prog*. 2001;97(3):45–53.
23. modeFRONTIER:The Multi-Objective Optimization and Design Environment. http://www.esteco.it; 2008.
24. Boyd S, VandenBerghe L. *Convex Optimization*. Cambridge University Press 2004.

25. Papalambros PI, Wilde DJ. *Principles of Optimal Design: Modeling and Computation*. Cambridge University Press; 2000.
26. Dixon JW, Mood AM. A Method for Obtaining and Analyzing Sensitivity Data. *Journal of the American Statistical Association*. 1948;43:109–126.
27. Menter FR. Two-equation eddy-viscosity turbulence models for engineering applications. *AIAA J*. 1994;38:1598–1605.
28. Wilcox DC. *Turbulence Modeling for CFD*. 2nd ed. DCW Industries; 1998a.
29. Wilcox DC. Reassessment of the scale-determining equation for advanced turbulence models. *AIAA J*. 1988b;26:1299–1310.
30. Gopalarathnan A, Selig MS. Low speed natural-laminar-flow airfoils: case study in inverse airfoil design. *J Aircraft*. 2001;5:38.
31. Xu G, Sankar LN. Computational study of horizontal axis wind turbines. *J Sol Energy Eng*. 2000;5:122.
32. Lyon CA, Broere AP, Giguere P, Gopalarathnam A, Selig MS. *Summary of Low-Speed Airfoil Data*. SoarTech Publications; 1997:3.
33. Caradonna FX, Tung C. Experimental and analytical studies of a model helicopter rotor in hove. *Vertica*. 1981;5:149–161.
34. Holland JH. *Adaptation in Natural and Artificial Systems: An Introductory Analysis with Applications to Biology, Control and Artificial Intelligence*. 2nd ed. MIT Press; 1992.
35. Avriel M. *Nonlinear Programming: Analysis and Methods*. Dover Publishing 2003.
36. Neyer BT. A D-optimality-based sensitivity test. *Technometrics*. 1994;36:61–70.
37. Neyer BT. *Analysis of Sensitivity Tests, MLM-3736. EG&G Mound Applied Technologies, Miamisburg, Ohio*; 1992.
38. Kresta SM, Wood PE. The mean flow field produced by a 45° pitched blade turbine: changes in the circulation pattern due to off bottom clearance. *Can J Chem Eng*. 1983;71:42–53.

Manuscript received Mar. 4, 2008, revision received Oct. 31, 2008, and final revision received Dec. 12, 2008.